

Chain rigidity modification to promote the electrochemical performance of polymeric battery electrode materials

Zhihui Niu, Huaxi Wu, Lei Liu, Gaole Dai, Shiyun Xiong, Yu Zhao, and Xiaohong Zhang

Table of Contents

Experimental Procedures	2-4
Figure S1	5
Figure S2	6
Figure S3	6
Figure S4	6
Figure S5	7
Figure S6	7
Table S1	8
Figure S7	8
Figure S8	9
Figure S9	10
Figure S10	11
Figure S11	12
Figure S12	13
Figure S13	14
References	15
MALDI-TOF Mass spectrum of p-DPPZR1	16-17
MALDI-TOF Mass spectrum of p-DPPZR2	18-19
MALDI-TOF Mass spectrum of p-DPPZR3	20-21
MALDI-TOF Mass spectrum of DPPZR1	22
MALDI-TOF Mass spectrum of DPPZR2	23
MALDI-TOF Mass spectrum of DPPZR3	24

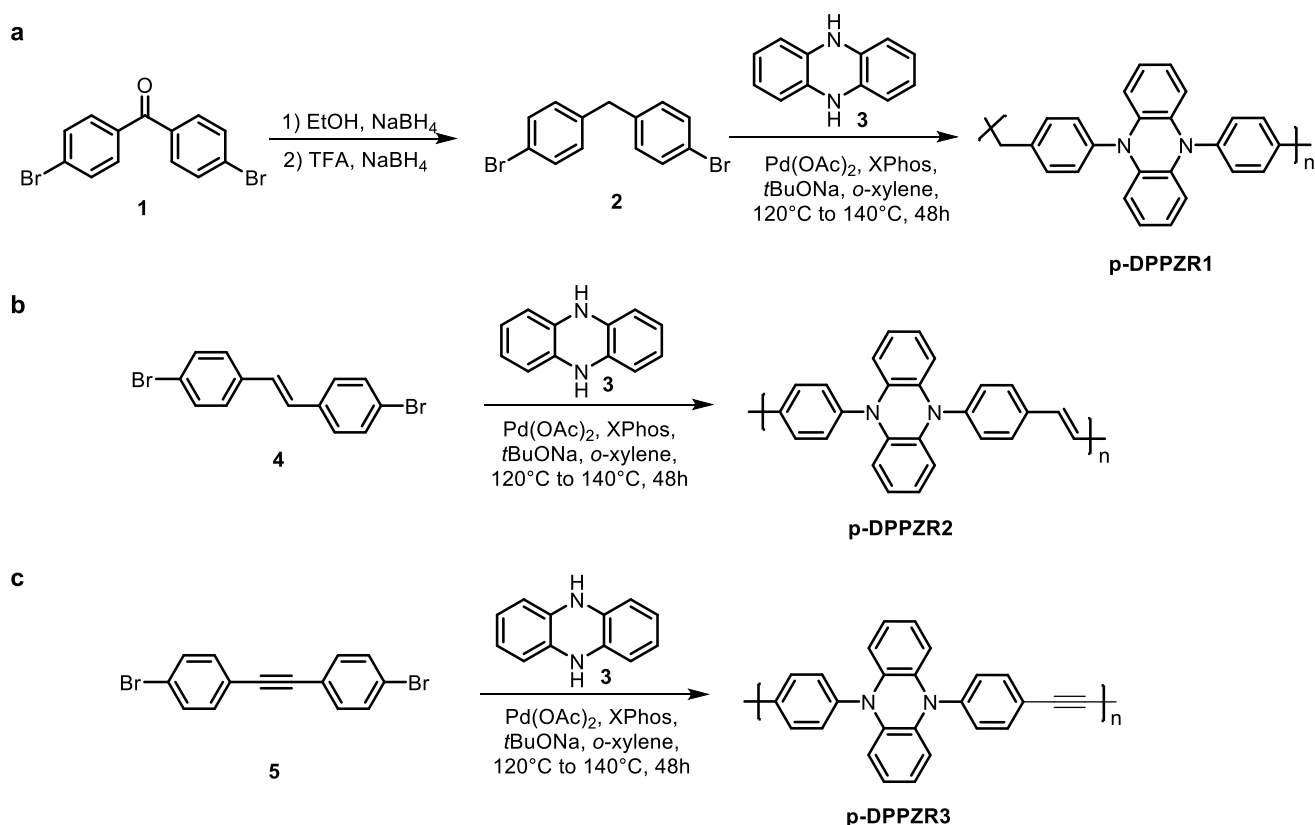
Experimental Procedures

General characterization information

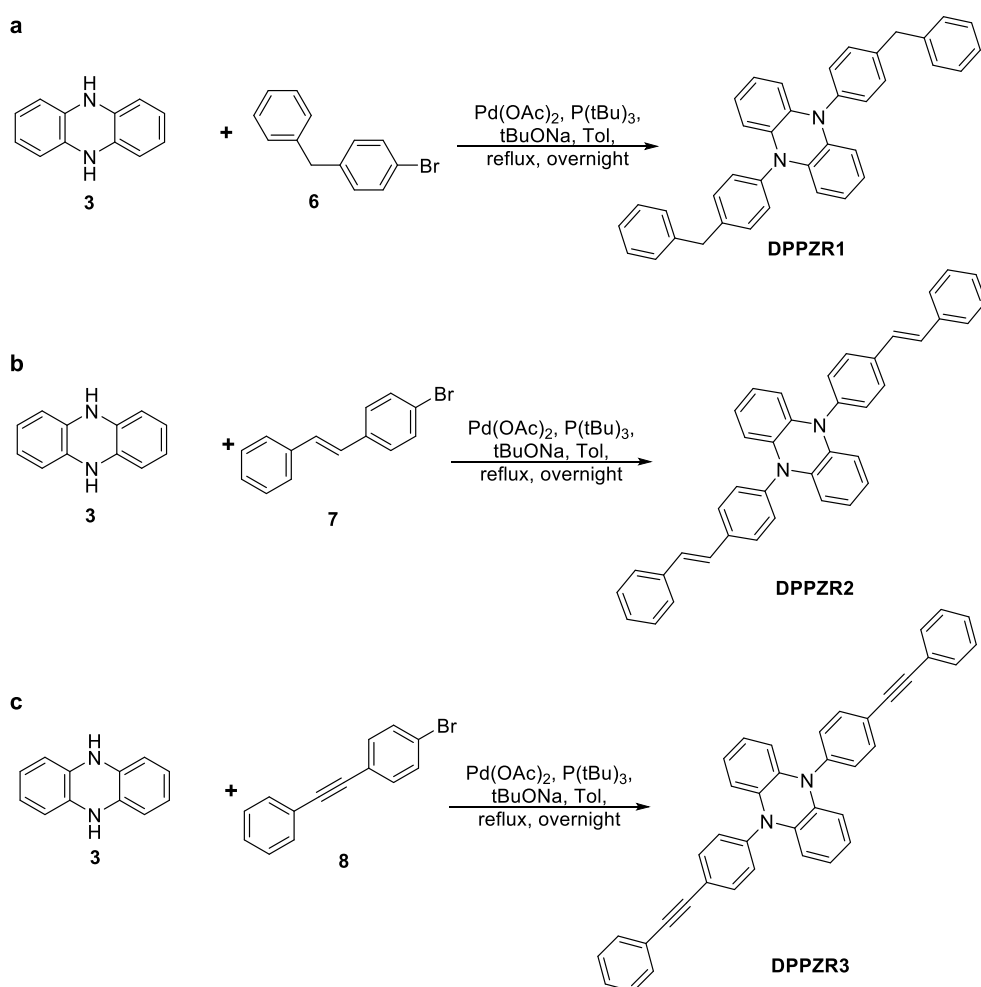
^1H and ^{13}C NMR spectra were recorded using Advance 500 MHz Bruker spectrometer with tetramethylsilane (TMS) as the internal standard. The chemical shift was recorded in ppm and the following abbreviations were used to explain the multiplicities: s = singlet, d = doublet, t = triplet, m = multiplet, br = broad. Column chromatography was performed on silica gel (200-300 mesh). MALDI-TOF mass spectra were recorded on a Bruker Ultraflextreme instrument. Thermogravimetric analysis (TGA) and Differential scanning calorimeter (DSC) measurements were carried out on a METTLER TA instrument at a heating rate of $10\text{ }^\circ\text{C min}^{-1}$ under nitrogen or air flow. The morphologies of the sample was observed using a scanning electron microscope (SEM, Zeiss Supra 55). Brunauer-Emmett-Teller (BET) surface area measurement (Micromeritics ASAP 2000) was estimated with N_2 used as the adsorptive gas at 77.35 K. Electrical conductivity was measured on BroadBand Dielectric Spectrometer (Novocontrol Concept80). Wettability tests were carried out on Contact angle system (Dataphysics OCA). The 2D GIXRD patterns were obtained on the BL14B1 beam line ($\lambda = 1.24\text{ \AA}$) at Shanghai Synchrotron Radiation Facility (SSRF). The sample-to-detector distance was 340 mm, the incidence angle was 0.16° , and the exposure time was 100–150 s. Numerical integration of the diffraction peak areas was performed with the software Fit2D. RDE studies were carried out on a rotating disk electrode (RRDE-3A, ALS Co. Ltd.) in a three-electrode cell with a glassy carbon electrode as the working electrode, a Pt wire as the counter electrode and an AgCl/Ag electrode as the reference electrode. Galvanostatic charge/discharge tests and other electrochemical characterizations were performed on an Arbin potentiostat (BT-2043, Arbin instruments).

Materials

All reagents were purchased from commercial sources without further purification. Anhydrous *o*-xylene were distilled from sodium-benzophenone immediately prior to use. 5,10-dihydrophenazine was prepared by previous literature procedures.¹



Scheme S1. Preparation routes to (a) p-DPPZR1, (b) p-DPPZR2 and (c) p-DPPZR3.



Scheme S2. Preparation routes to (a) DPPZR1, (b) DPPZR2 and (c) DPPZR3.

Electrode preparation and cell assembly

For a typical electrode preparation, the as-prepared polymer, Super P carbon (Timcal Graphite & Carbon), and polyvinylidene fluoride binder (Fisher Scientific) dissolved in *N*-methyl-2-pyrrolidone (anhydrous, Fisher Scientific) were mixed together. The weight ratio of PZDB-Li₂: Super P carbon: polyvinylidene fluoride was 7:2:1. The mixture was thoroughly stirred in a centrifugal mixer (Thinky ARE-300) for 30 min until a homogenous slurry formed. The slurry was then casted on Al foil with thickness of 50 μm, dried in vacuum at 80 °C for 12 h, and pressed at 1 MPa·cm⁻². The thickness of the active material was 35±2 μm. The average mass loading for each electrode was ca. 1.0 mg·cm⁻² for p-DPPZR1 and p-DPPZR2, and 0.5 mg·cm⁻² for p-DPPZR3. The cell was assembled in a glove box (H₂O and O₂ concentration < 1ppm) using a standard CR2032 coin cell, in which metallic lithium was used as the anode, Celgard 2500 as the separator, and 1 M LiPF₆ in EC/DEC (1:1, v:v) as the electrolyte. Galvanostatic experiments were performed on a battery testing system (BT-2043, Arbin Instruments) at room temperature. The cut-off potentials were set to 2.5 – 4.3 V.

Identification of surface capacitive effect and diffusion-controlled insertion process

Sweep-rate-dependent cyclic voltammetry (CV) was used to distinguish quantitatively the faradaic contribution from the PF₆⁻ insertion process to the current response.² The CV profiles were recorded on a coin cell with a p-DPPZR1 or p-DPPZR2 or p-DPPZR3 positive electrode and a metallic Li negative electrode at room temperature. The total stored charge can be separated into i) the faradaic contribution from the PF₆⁻ insertion process, ii) the faradaic contribution from pseudocapacitance,³ and iii) the nonfaradaic contribution from the double layer effect. Thus, the current response at a fixed potential was the combination of i) and ii), which could be expressed as:⁴

$$i(V) = k_1v + k_2v^{1/2}$$

where k_1v and $k_2v^{1/2}$ correspond to the current contributions from the surface capacitive effects and the diffusion-controlled intercalation process, respectively. It's possible to quantify the fraction of the current due to each of these contributions at specific potentials by determining k_1 and k_2 , which could be obtained from the plot of $i(V)/v^{1/2}$ vs. $v^{1/2}$.

RDE study

All linear sweep voltammetry (LSV) experiments were carried out on a rotating disk electrode (RRDE-3A, ALS Co. Ltd.) in a three-electrode cell. The glassy carbon electrode (3 mm in diameter) was rotated at 900, 1225, 1600, 2025, 2500, 3025, 3600,

4225, 4900 and 5625 r.p.m., while the voltage was linearly swept from 0 to 1.2 V (vs. AgCl/Ag) at a sweep rate of 10 mV·s⁻¹. Koutecký-Levich plots at the reciprocal of the current at low over potential (5, 10, 15, 20, 30, 40, 60 and 80 mV) were fitted a straight linearly relationship with the reciprocal of the square root of the rotation rate. The y-intercept give the reciprocal of i_k , the current in the absence of mass transport limitations (the extrapolation to infinite rotation rate). A plot of $\lg i_k$ versus overpotential give a fitting line with x-intercept as the log of the exchange current i_0 . The electron-transfer rate constant (k_0) was calculated according to Butler-Volmer equation: ⁵

$$i_0 = nFAk_0C_0$$

where n is the number of electrons transferred in the redox reaction ($n=1$ in all cases), F is the Faraday constant (96485 C mol⁻¹), A is the surface area of the rotating electrode (0.0707 cm²), and C_0 is the concentration of the active materials (0.5 mM for DPPZR1, and 0.1 mM for DPPZR2 and DPPZR3).

Diffusivity measurement

GITT measurement was performed on a coin cell with a p-DPPZR1 or p-DPPZR2 or p-DPPZR3 positive electrode and a metallic Li negative electrode at room temperature. Prior to the measurement, the cell was fully charged and discharged at a current rate of 0.5 C. The GITT current input consisted of 20 discharge pulses. Each pulse lasts 8 minutes followed by 60 minutes relaxation. The solid phase diffusivity of PF₆⁻ in PZDB-Li₂ (D) was calculated using the GITT diffusivity formula: ⁶

$$D = \frac{4}{\pi\tau} \left(\frac{n_M V_M}{S} \right)^2 \left(\frac{\Delta V_s}{\Delta V_t} \right)^2$$

where n_M and V_M are the mass (mol) and molar volume (cm³·mol⁻¹) of the active material, respectively, S is the interfacial area of the active material (cm²), τ is the time duration of the pulse (s), ΔV_s is the difference between the steady-state potentials before and after a current pulse and thus indicates the change in the potential due to thermodynamics, and ΔV_t is the magnitude of the potential changes (without the IR drop) during the current pulse.

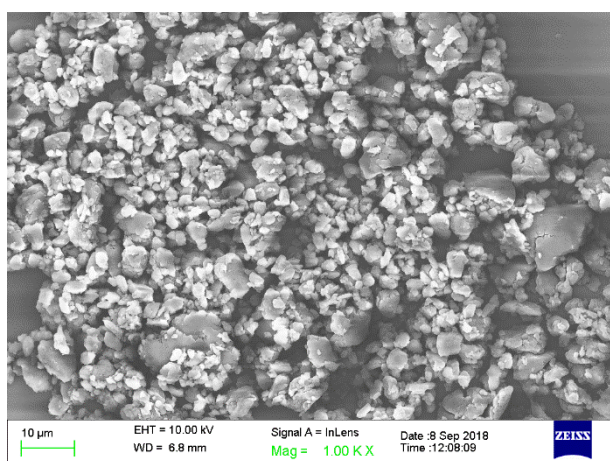
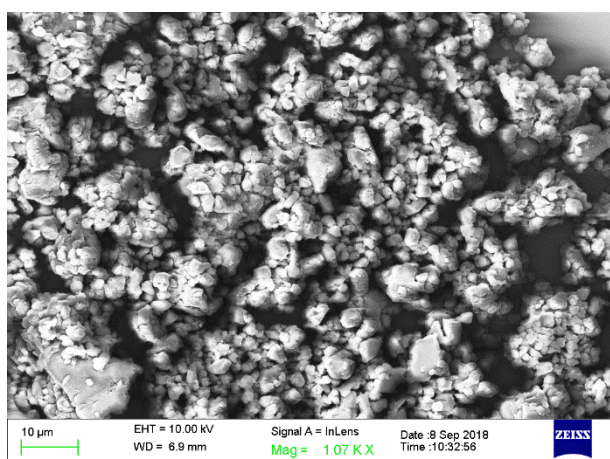
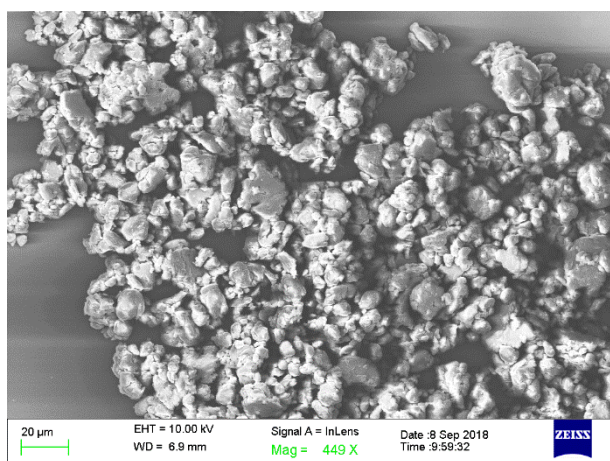


Figure S1. SEM images of the as-synthesized p-DPPZR1 (top), p-DPPZR2 (middle) and p-DPPZR3 (bottom).

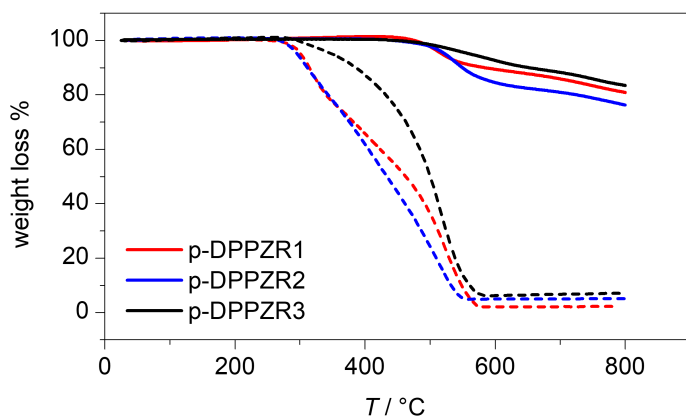


Figure S2. TGA analysis of the as-synthesized polymers in N₂ (solid lines) and in air (dash lines) at a heating rate of 10 °C·min⁻¹.

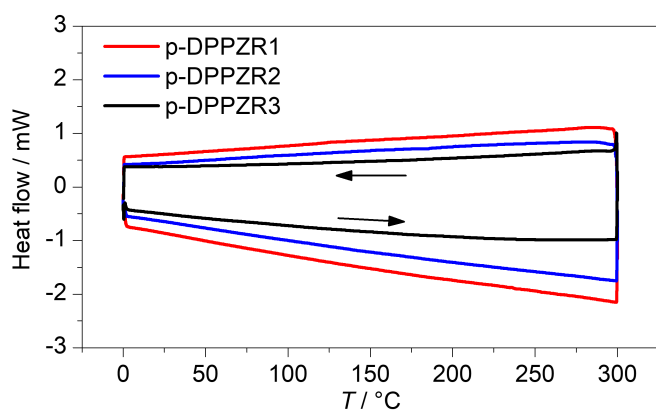


Figure S3. DSC analysis of the as-synthesized polymers in N₂ in the temperature range of 0–300 °C at a heating rate of 10 °C·min⁻¹.

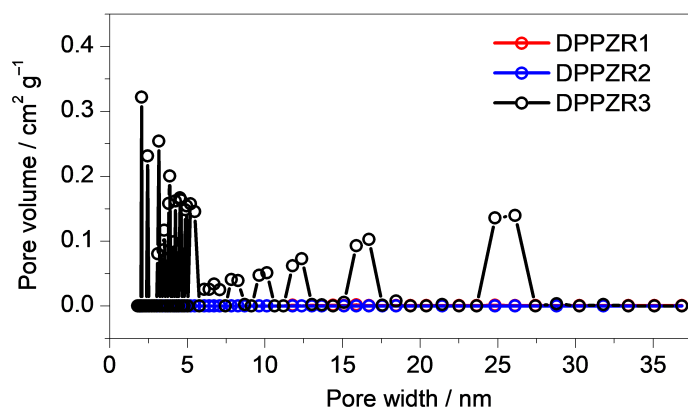


Figure S4. Pore size distributions of the as-synthesized polymers.

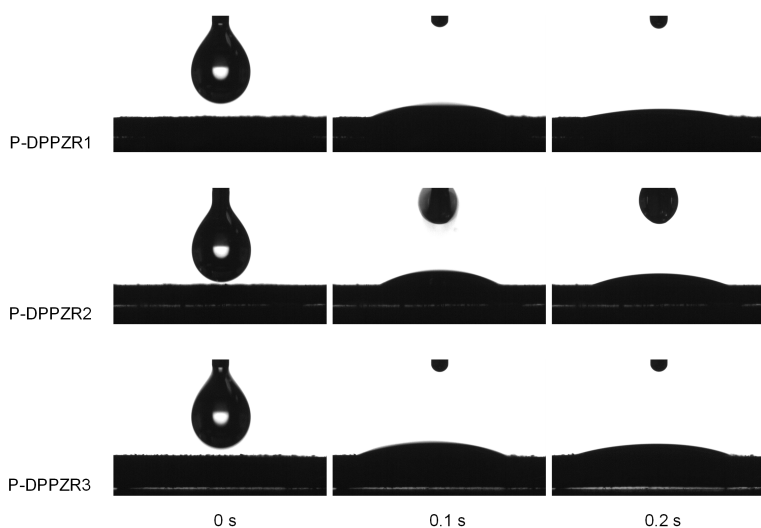


Figure S5. Wettability tests of organic electrolyte (1 M LiPF₆ in EC/DEC, 1:1, v:v) on p-DPPZR1, p-DPPZR2 and p-DPPZR3 electrodes.

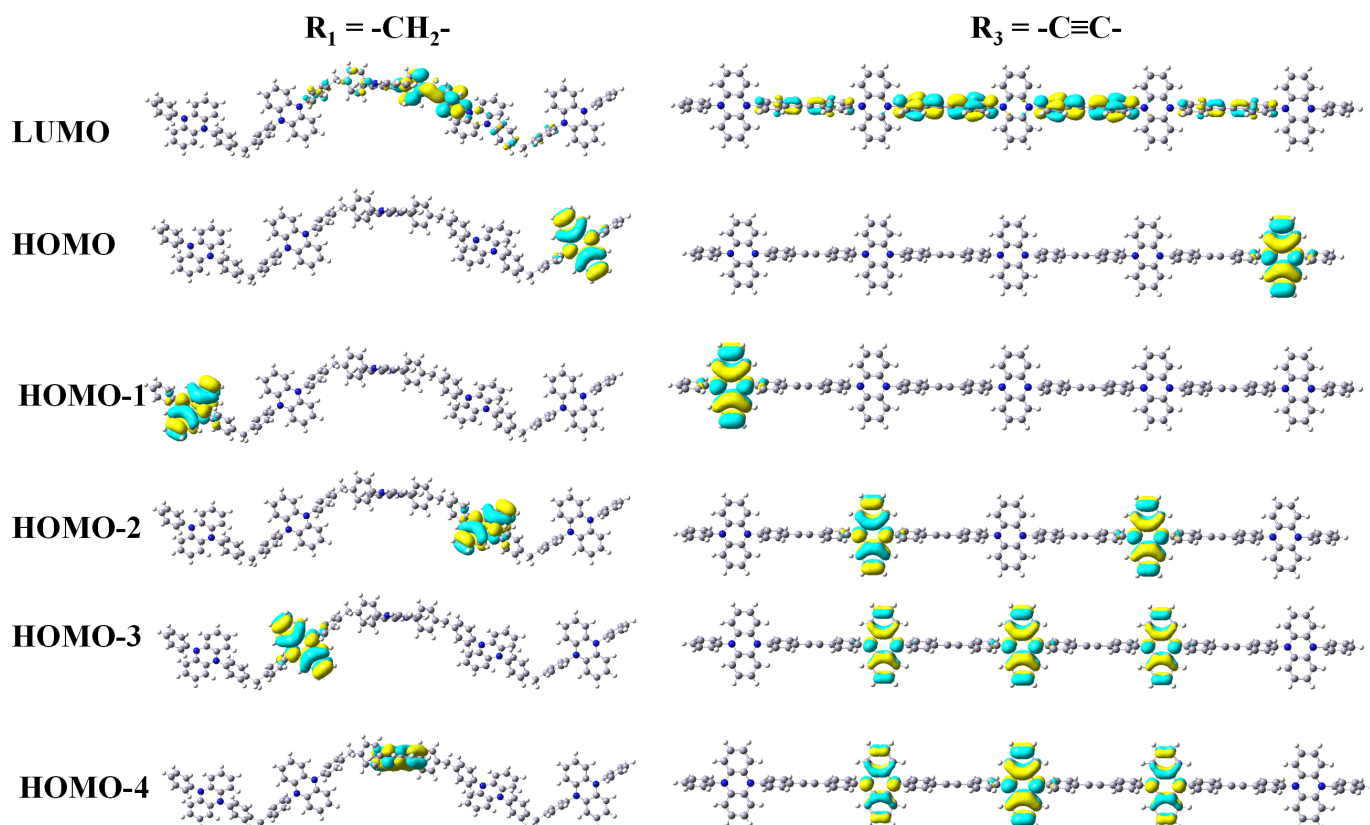


Figure S6. The frontier molecular orbital of p-DPPZR1 and p-DPPZR3. The results show that the HOMO orbital distributed on the central N-containing heterocyclic of DPPZ unit rather than the bridging atoms or functional groups, similar with the DPPZ monomer.

Table S1 The molecular orbital energy level of DPPZ monomer and DPPZ polymers.

Bridge	-CH ₂ -	-CH=CH-	-C≡C-	Monomer
LUMO	-0.576	-1.788	-1.701	-0.374
Gap	3.505	2.326	2.451	3.632
HOMO	-4.081	-4.114	-4.151	-4.006
HOMO-1	-4.082	-4.114	-4.151	
HOMO-2	-4.090	-4.152	-4.219	
HOMO-3	-4.095	-4.152	-4.219	
HOMO-4	-4.103	-4.156	-4.225	
Gap	1.574	1.552	1.517	1.657
HOMO-5	-5.677	-5.708	-5.742	-5.663
HOMO-6	-5.678	-5.708	-5.742	
HOMO-7	-5.686	-5.742	-5.804	
HOMO-8	-5.690	-5.742	-5.804	
HOMO-9	-5.694	-5.746	-5.81	

The molecular orbital energy level analysis indicates that the energy levels from HOMO to HOMO-4 (corresponding to p-DPPZ with five DPPZ units at the valence state of +1, +2, +3, +4 and +5) are in the same order of magnitude, indicating the first oxidation potential of the p-DPPZ is almost identical. Similarly, the energy level from HOMO-5 to HOMO-9 (corresponding to p-DPPZ with five DPPZ units at the valence state of +6, +7, +8, +9 and +10) are also similar. The energy gaps (HOMO-4 – HOMO-5) of the first oxidation and the second oxidation of p-DPPZ are similar with those of corresponding DPPZ monomers.

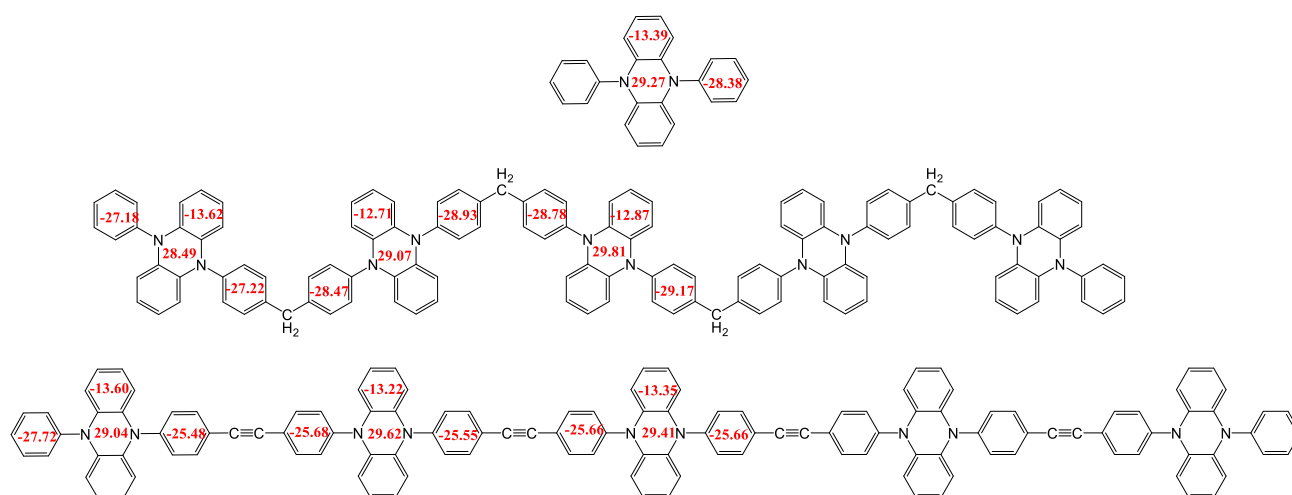


Figure S7. Calculated NICS(1)zz values of p-DPPZR1 and p-DPPZR3. NICS values were calculated using the standard GIAO (NMR=GIAO).⁷ To obtain the best NICS aromaticity index, NICS(1)zz values were selected.⁸ The DPPZ units on the edge of p-DPPZ chain exhibit relatively weak aromaticity, indicating the redox reaction at each oxidation step should occur preferably on the edge and then in the center. Such a trend is in consistent with the gradually increased HOMO energy levels of the corresponding p-DPPZ in the molecular orbital analysis shown in Table S1.

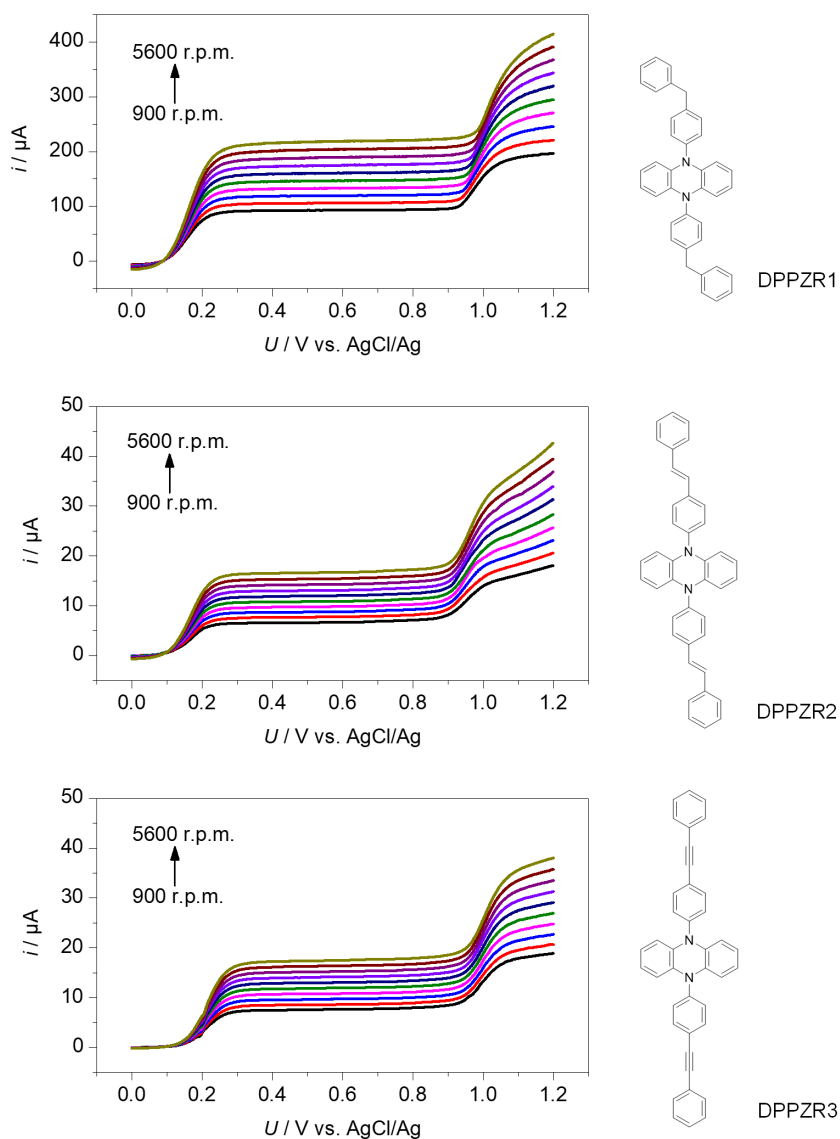


Figure S8. RDE profiles of DPPZR1, DPPZR2 and DPPZR3 (corresponding to the repeating unit of p-DPPZR1, p-DPPZR2 and p-DPPZR3, respectively) at a rotation speed of 900, 1225, 1600, 2025, 2500, 3025, 3600, 4225, 4900 and 5600 r.p.m. and a sweeping rate of $10 \text{ mV}\cdot\text{s}^{-1}$. The electrolyte is composed of 0.5/0.1/0.1 mM and 0.1M LiTFSI in EC/DEC.

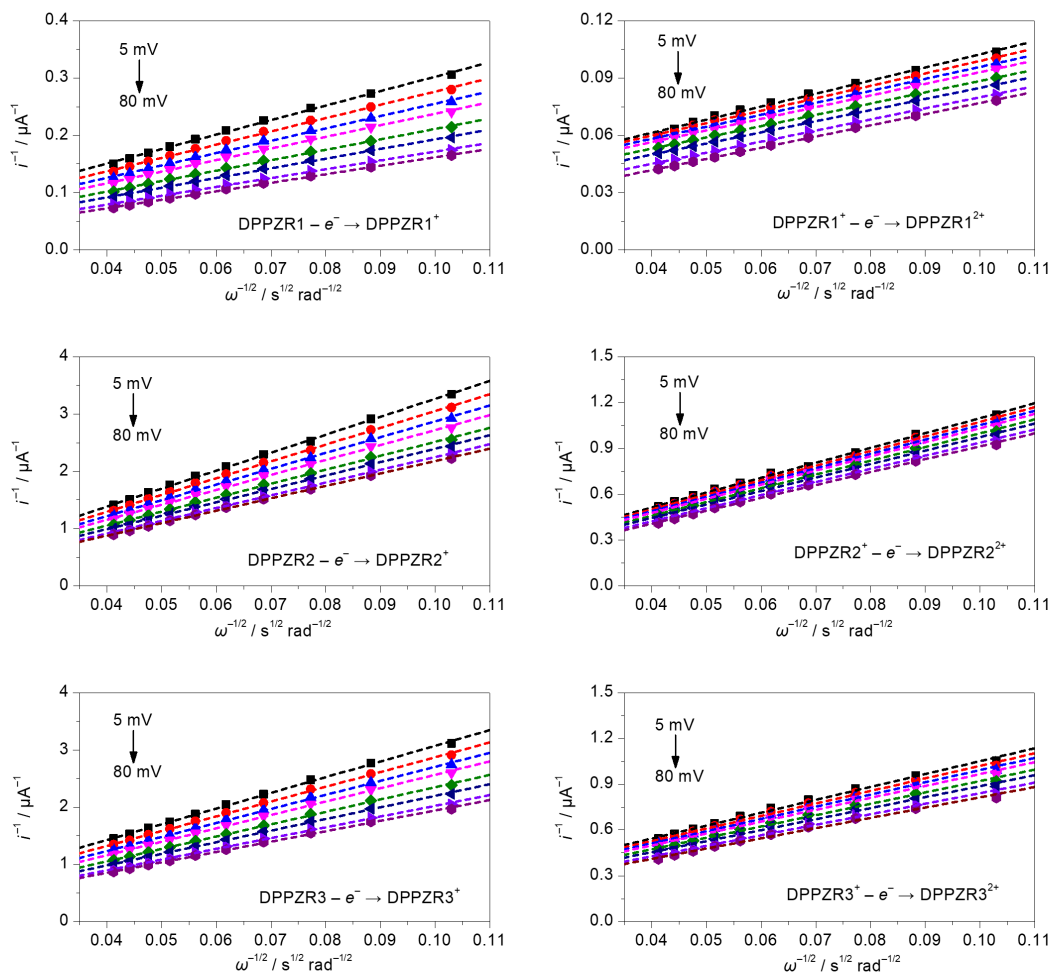


Figure S9. Koutecký-Levich plots of DPPZR1, DPPZR2 and DPPZR3 at overpotentials of 5, 10, 15, 20, 30, 40, 60 and 80 mV.

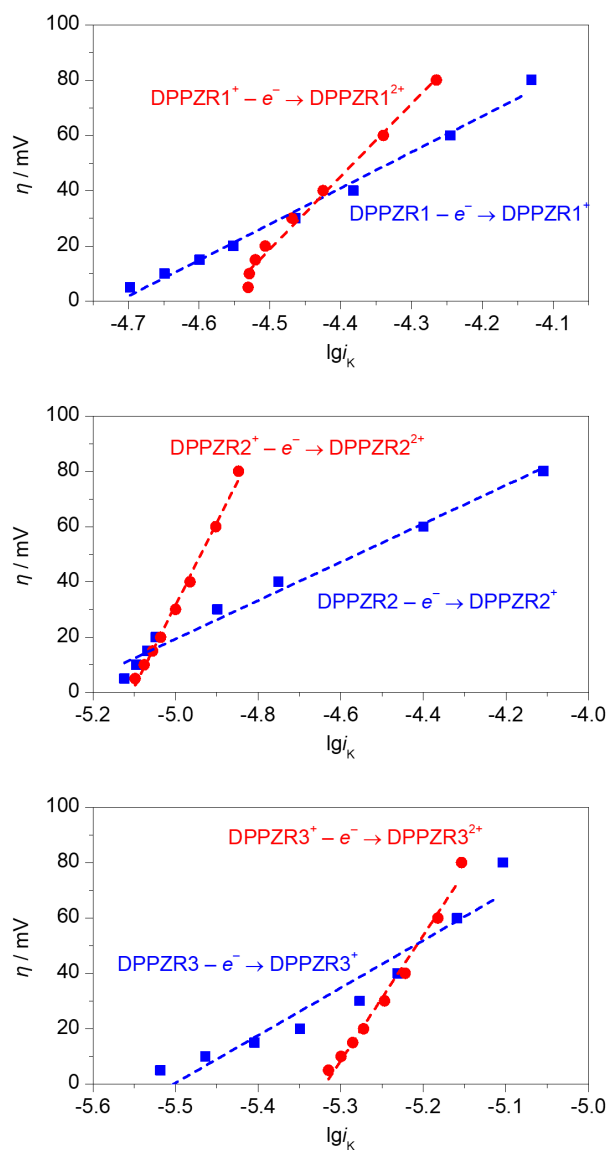


Figure S10. Overpotential (η) as a function of the logarithm of kinetic current (i_k) of DPPZR1, DPPZR2 and DPPZR3. The calculated electron-transfer rate constant of DPPZR1, DPPZR2 and DPPZR3 are 5.7×10^{-3} , 7.7×10^{-3} and $4.6 \times 10^{-3} \text{ cm} \cdot \text{s}^{-1}$ upon the first oxidation, and 7.9×10^{-3} , 1.2×10^{-2} and $7.0 \times 10^{-3} \text{ cm} \cdot \text{s}^{-1}$ upon the second oxidation, respectively.

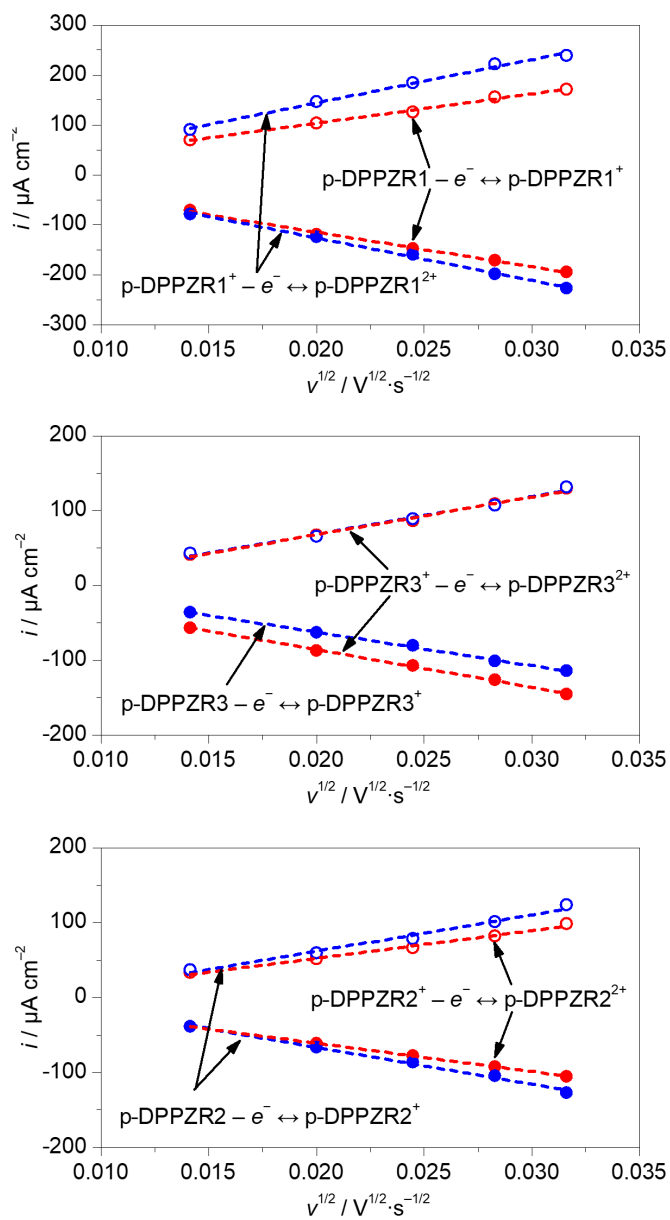


Figure S11. Cathodic/anodic peak current versus the square root of the sweeping rate of p-DPPZR1, p-DPPZR2 and p-DPPZR3.

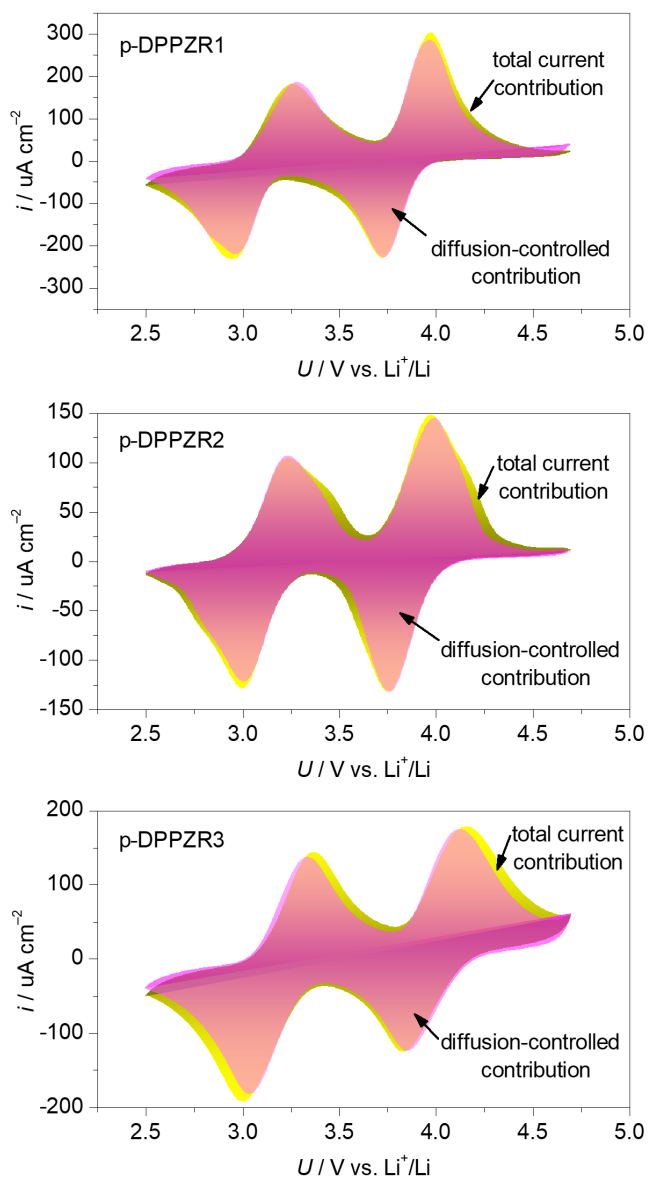


Figure S12. Voltammetry response at a sweeping rate of 1 mV s^{-1} of the p-DPPZR1, p-DPPZR2 and p-DPPZR3 electrodes. The yellow and pink regions represent the contributions from the total current and the calculated diffusion current, respectively. The integrated area of diffusion-controlled contribution occupies 94.9%, 92.2% and 94.2% in the area of total current contribution for p-DPPZR1, p-DPPZR2 and p-DPPZR3, respectively.

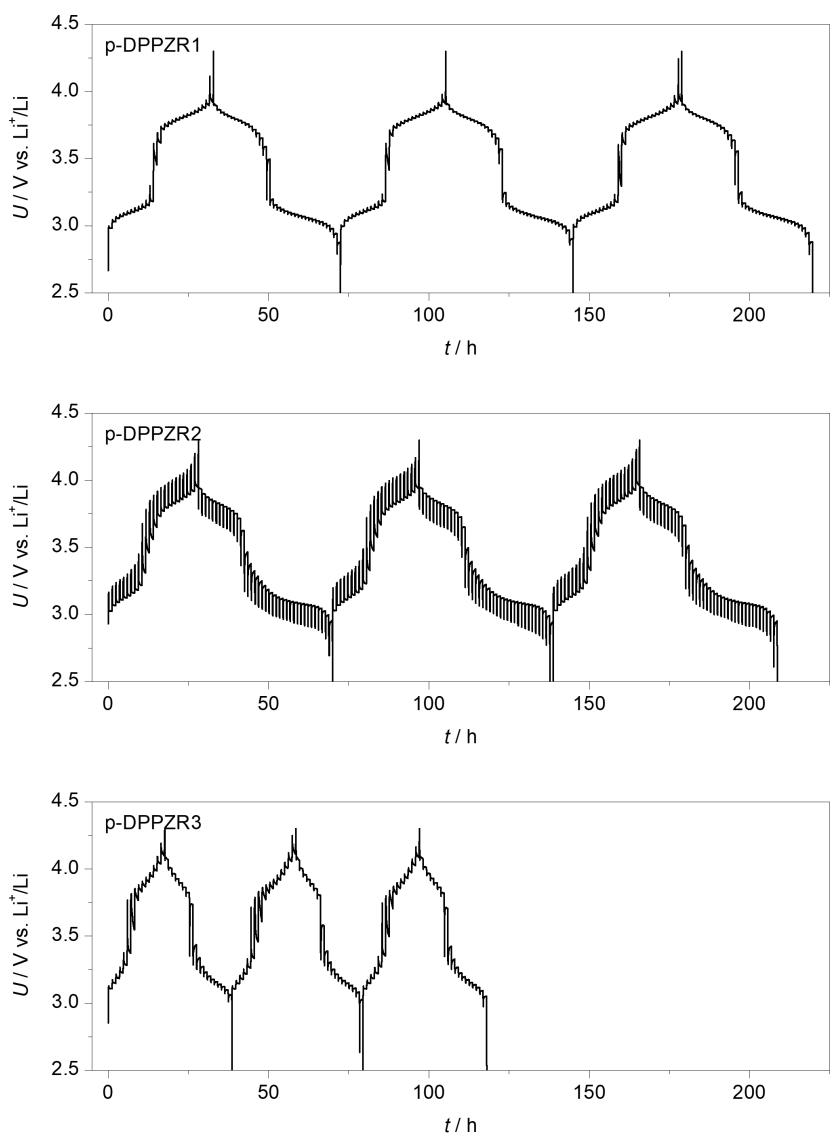
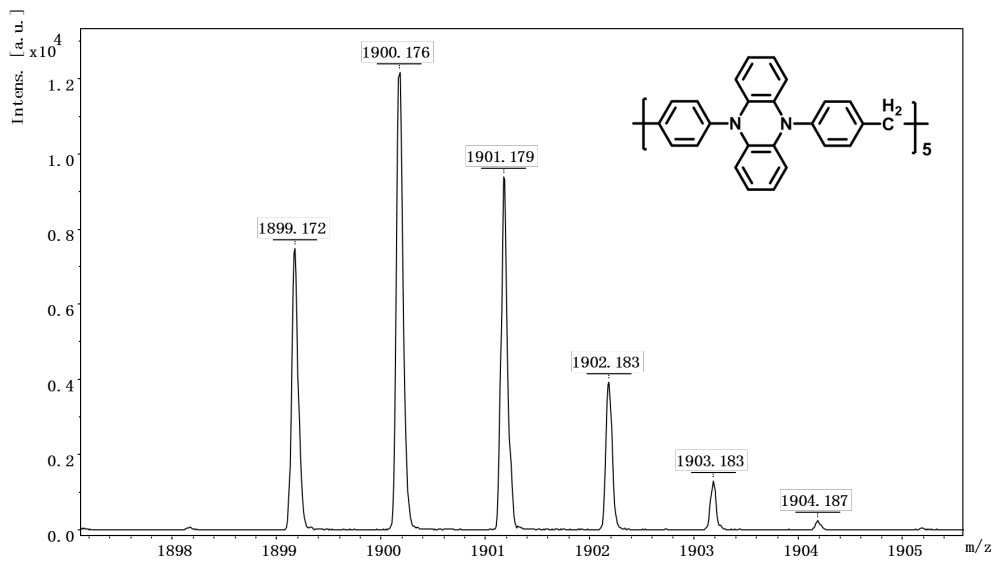
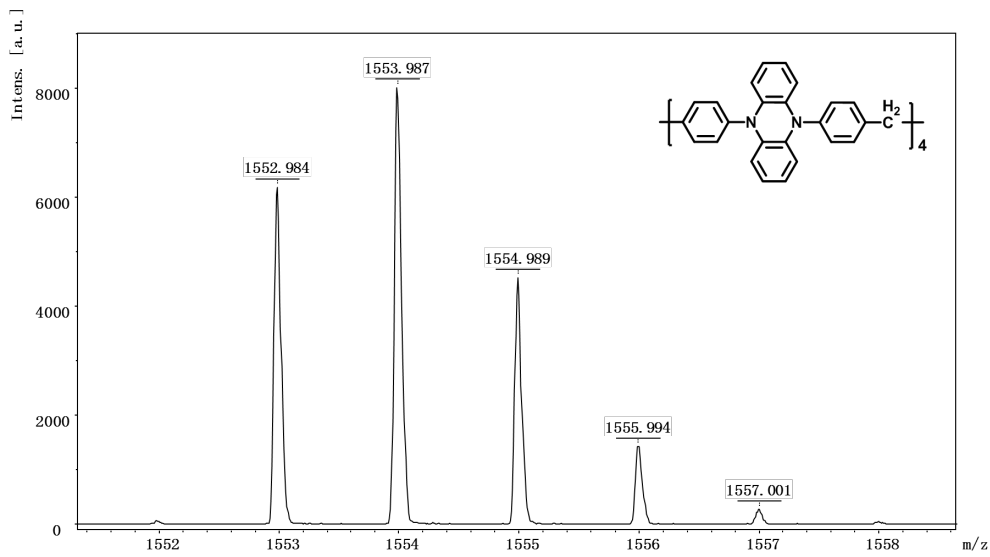
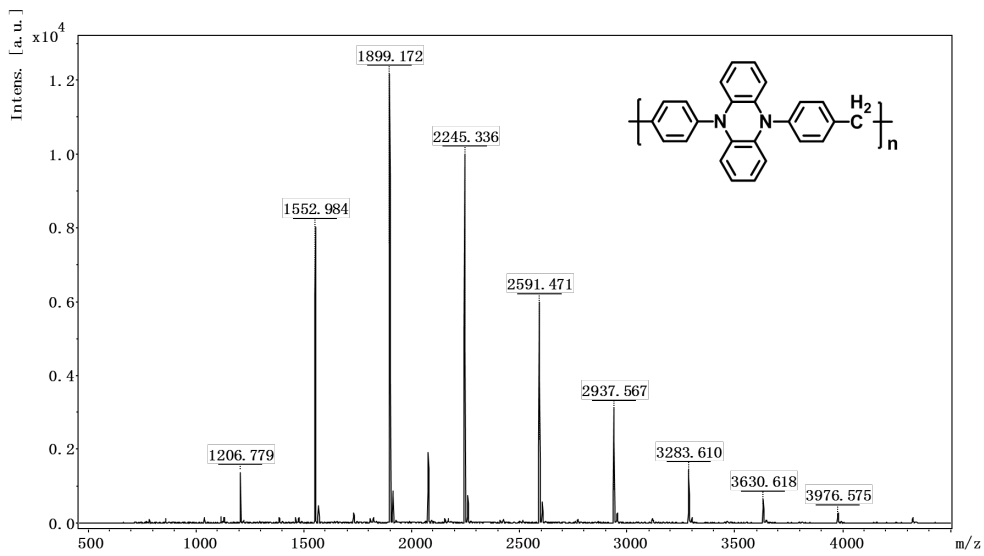
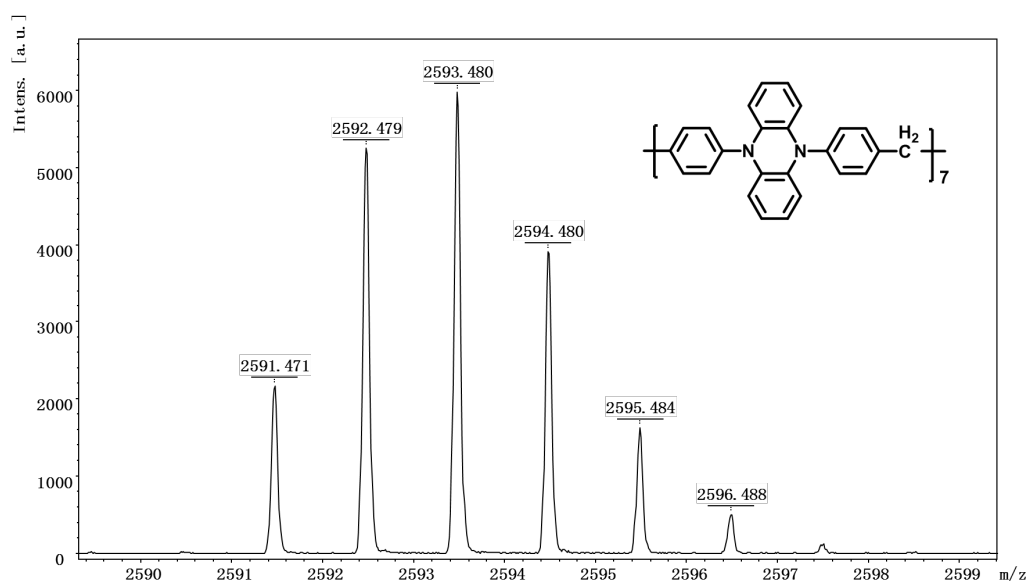
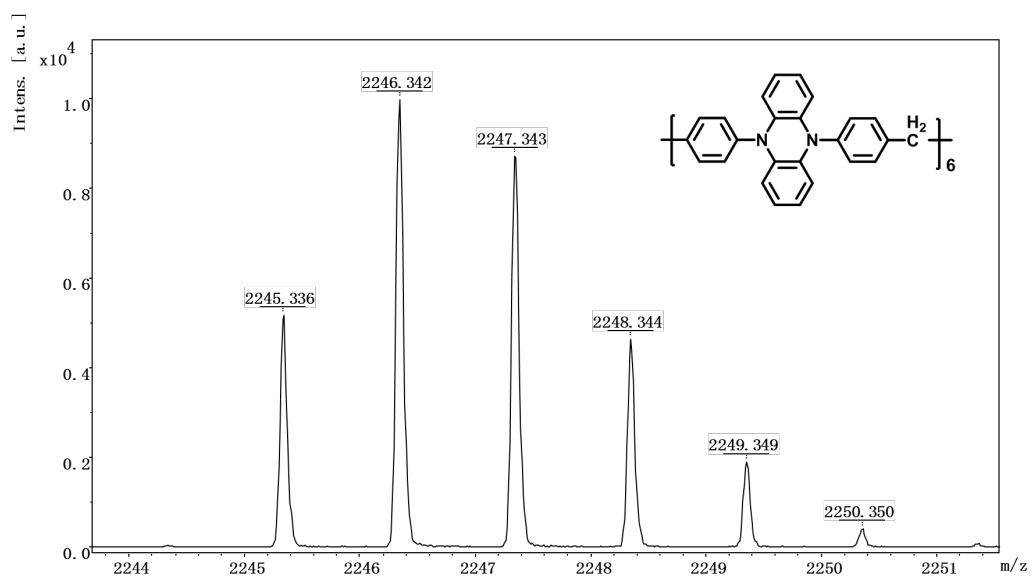


Figure S13. GITT curves of the p-DPPZR1, p-DPPZR2 and p-DPPZR3 electrodes.

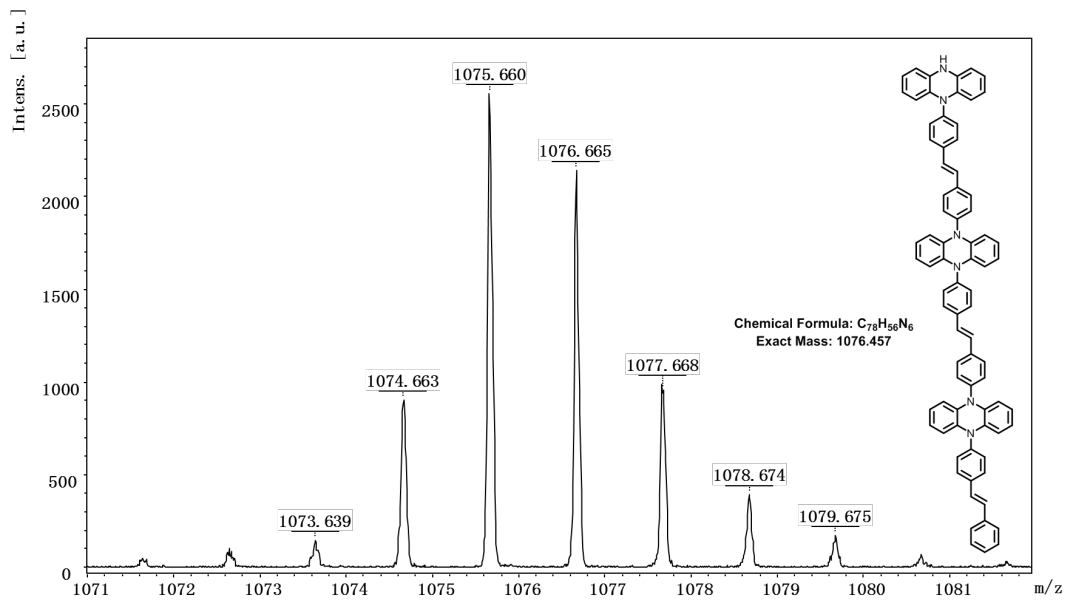
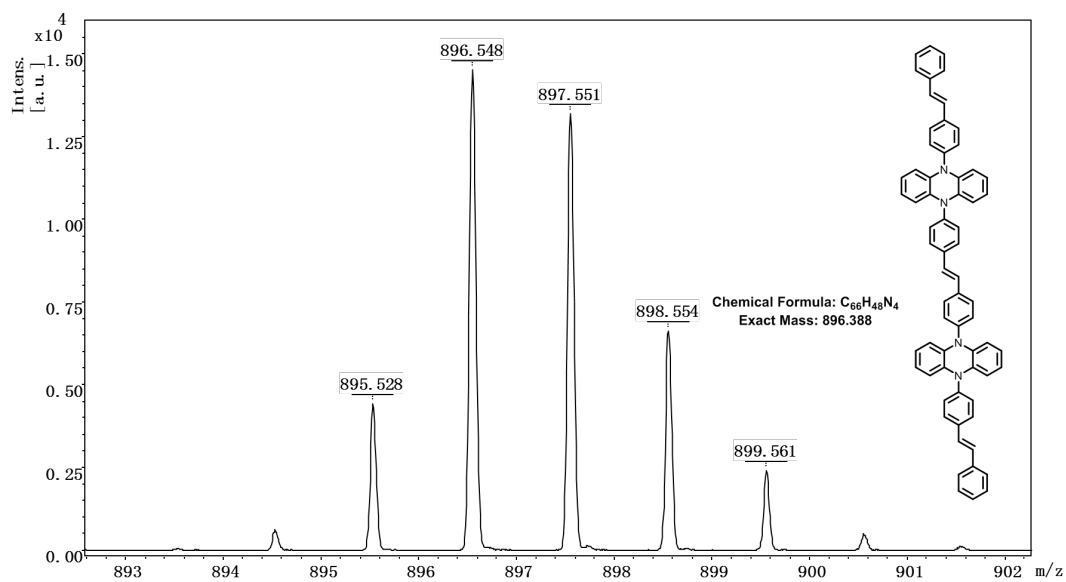
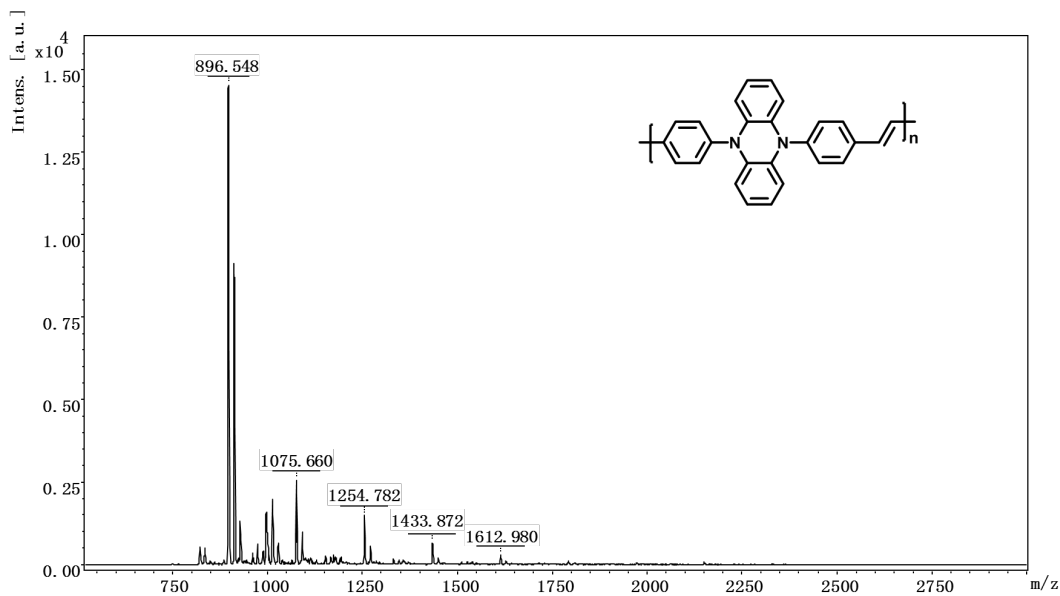
References

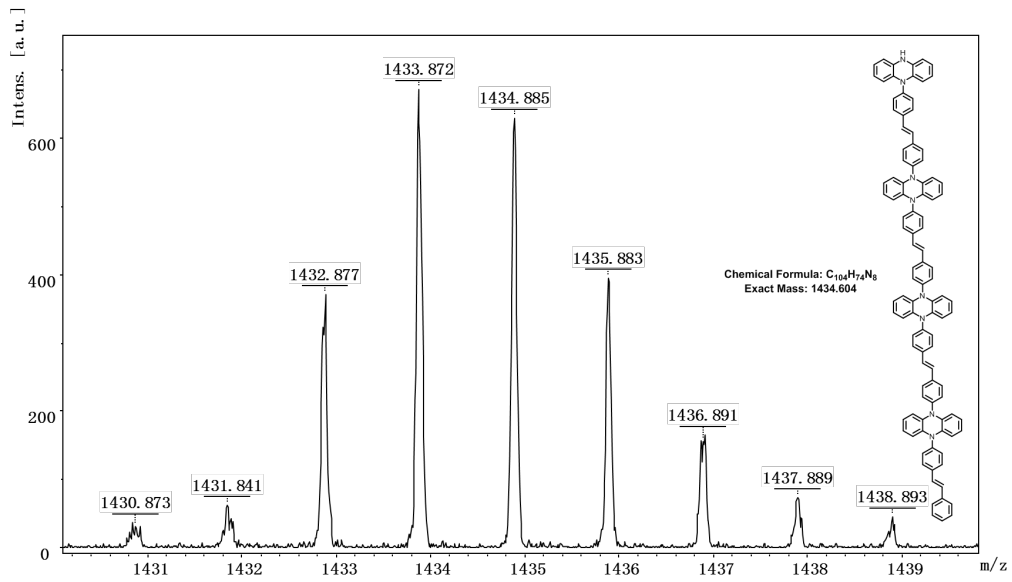
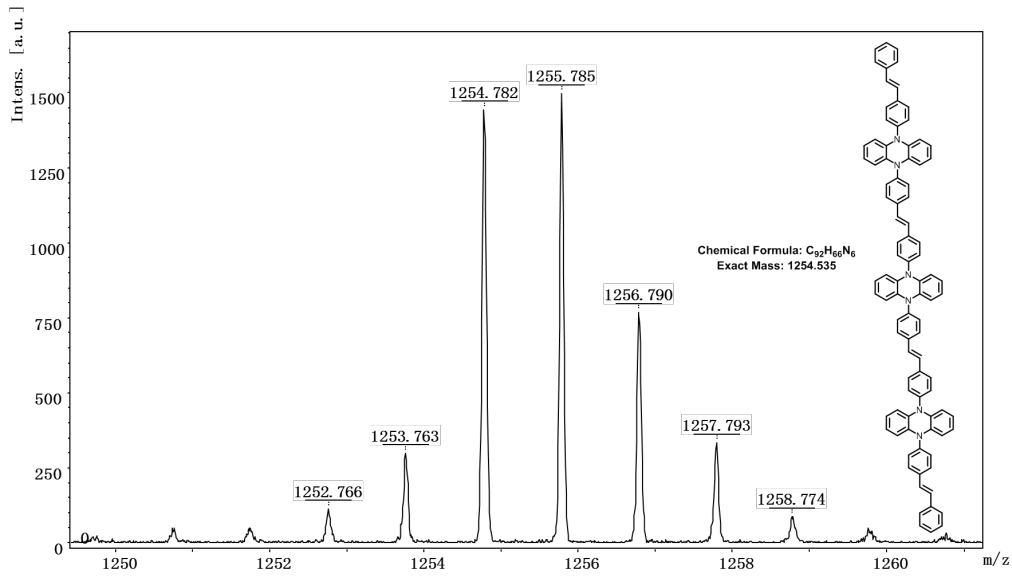
- [1] D. Koyama, H. J. A. Dale, A. J. Orr-Ewing, *J. Am. Chem. Soc.* **2018**, *140*, 1285–1293.
- [2] J. Wang, J. Polleux, J. Lim, B. Dunn, *J. Phys. Chem. C* **2007**, *111*, 14925–14931.
- [3] B. E. Conway, V. Birss, J. Wojtowicz, *J. Power Sources* **1997**, *66*, 1–14.
- [4] T. C. Liu, W. G. Pell, B. E. Conway, S. L. Roberson, *J. Electrochem. Soc.* **1998**, *145*, 1882–1888.
- [5] A. J. Bard, L. R. Faulkner, *Electrochemical Methods. Fundamentals and Applications* (2nd Ed). John Wiley & Sons, Inc, New York, **2001**.
- [6] Z. Shen, L. Cao, C. D. Rahn, C.-Y. Wang, *J. Electrochem. Soc.* **2013**, *160*, A1842–A1846.
- [7] Z. Chen, C. S. Wannere, C. Corminboeuf, R. Puchta, P. V. R. Schleyer, *Chem. Rev.* **2005**, *105*, 3842–3888.
- [8] H. Fallah-Bagher-Shaidei, S. S. Wannere, C. Corminboeuf, R. Puchta, P. V. R. Schleyer, *Org. Lett.* **2006**, *8*, 863–866.



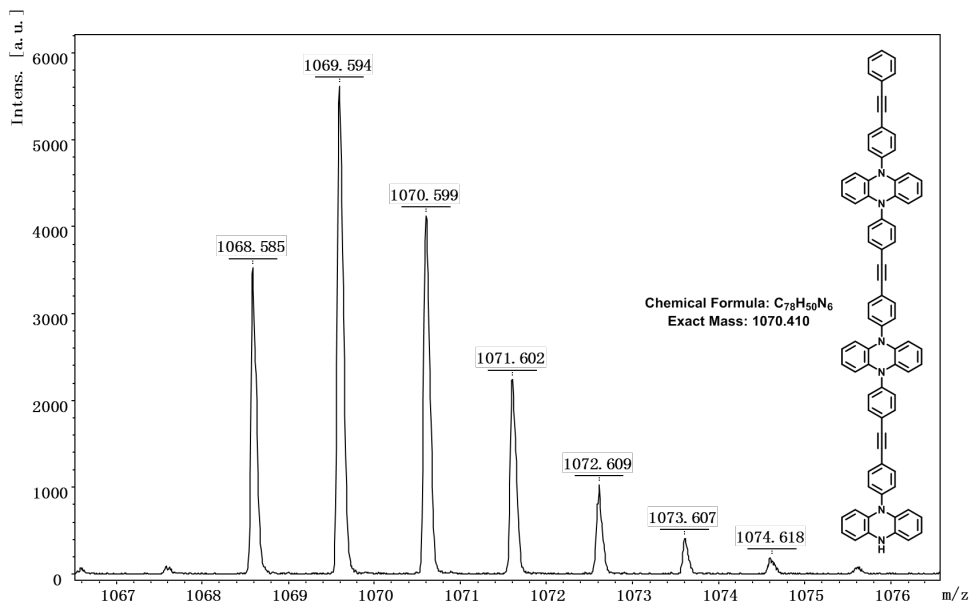
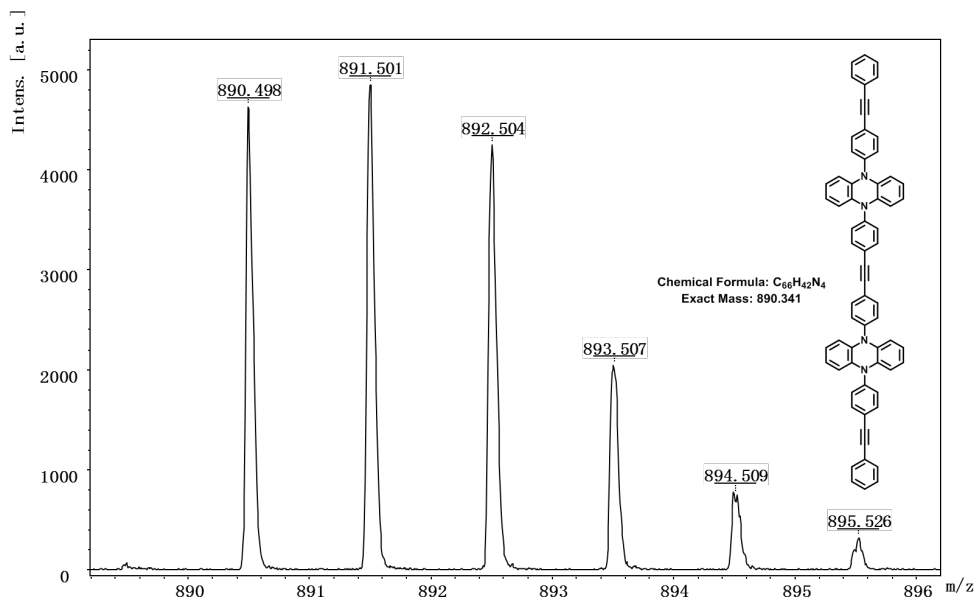
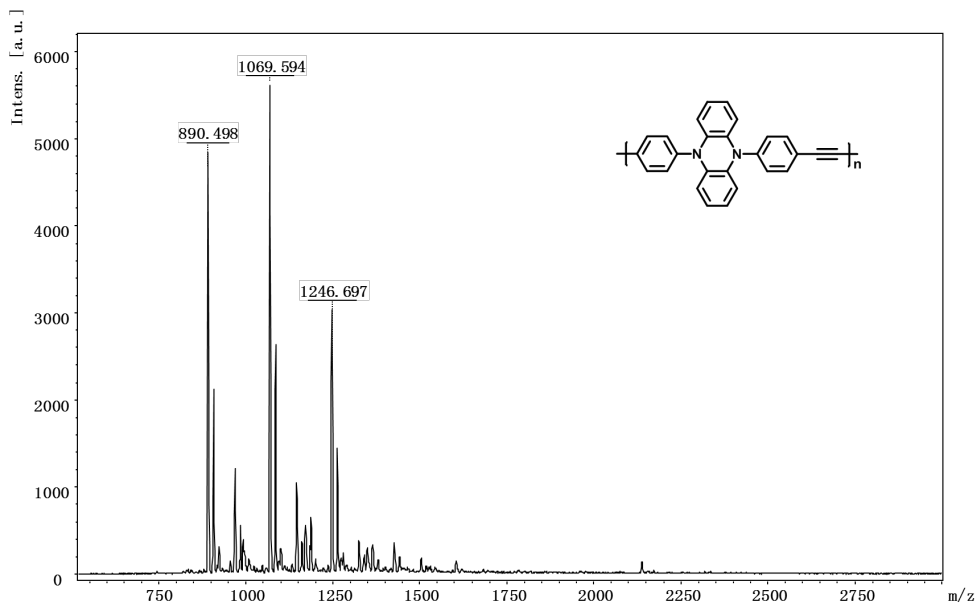


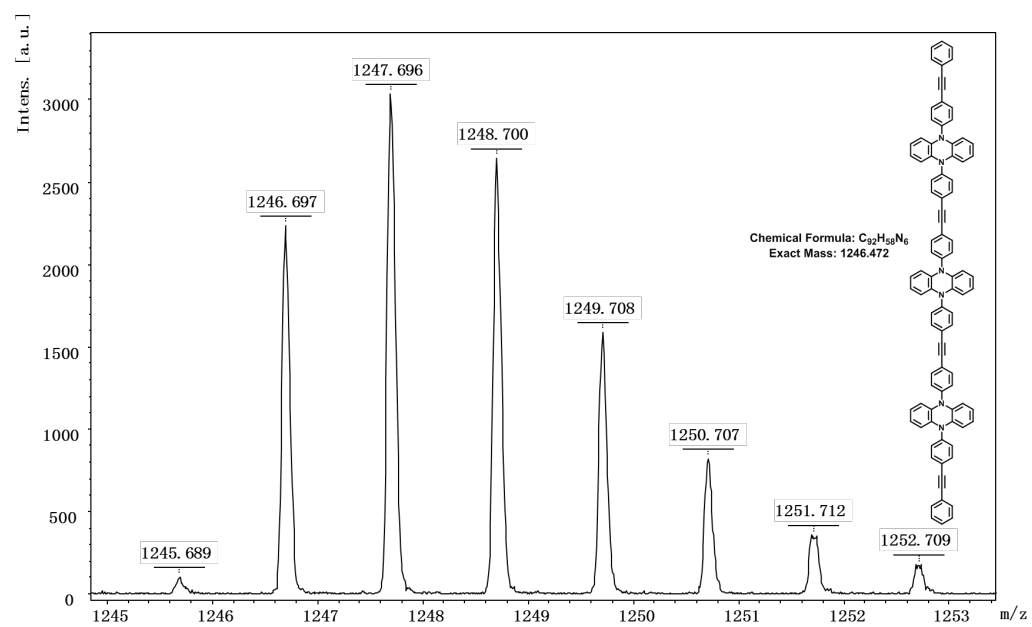
MALDI-TOF Mass spectrum of **p-DPPZR1**.



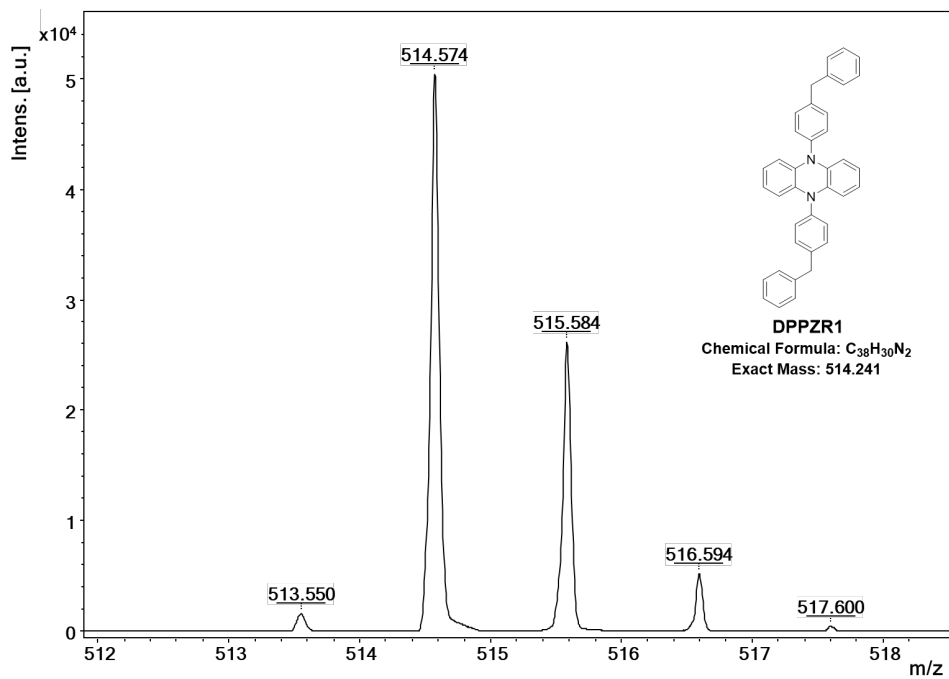


MALDI-TOF Mass spectrum of **p-DPPZR2**.

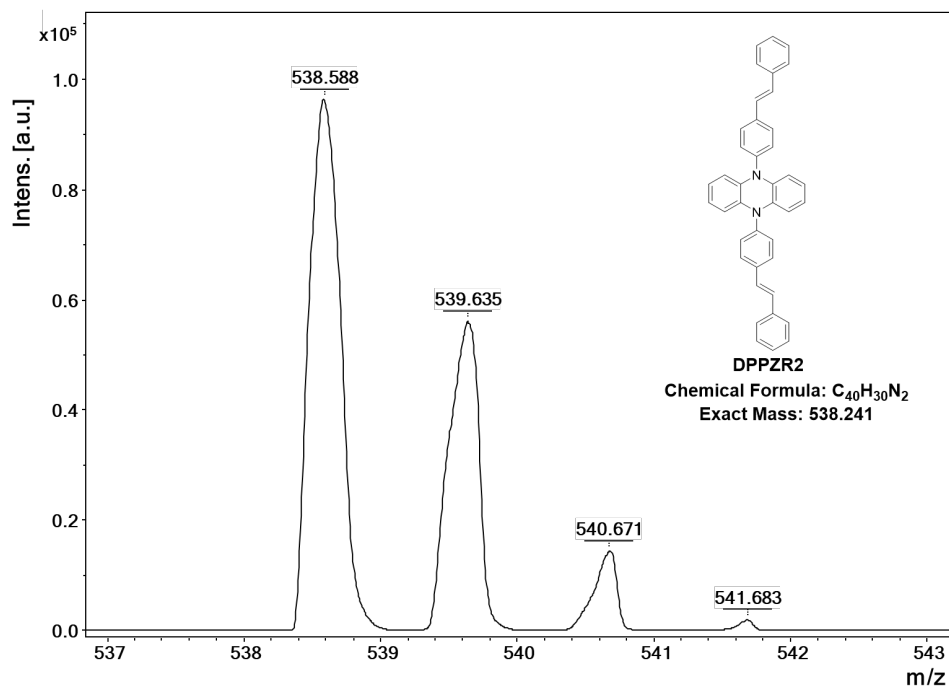




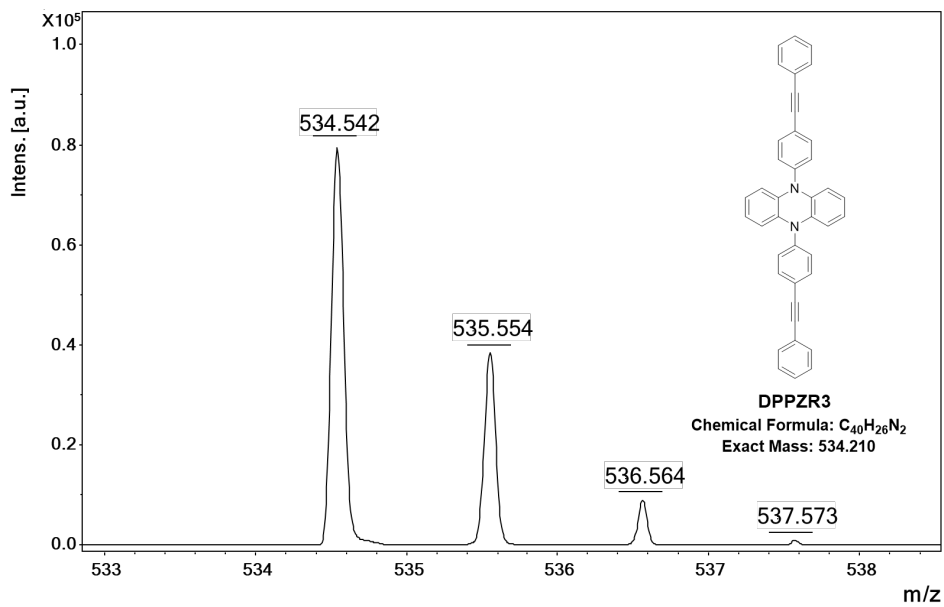
MALDI-TOF Mass spectrum of **p-DPPZR3**.



MALDI-TOF Mass spectrum of **DPPZR1**.



MALDI-TOF Mass spectrum of **DPPZR2**.



MALDI-TOF Mass spectrum of **DPPZR3**.